SAND2008-0011C

Force and Moment Measurements of a Transonic Fin-Wake Interaction

Justin A. Smith,[1] John F. Henfling,[2] Steven J. Beresh,[3] Thomas W. Grasser,[4] and Russell W. Spillers[5]
Sandia National Laboratories, P. O. Box 5800, Albuquerque, NM 87185

Force and moment measurements have been made on an instrumented subscale fin model at transonic speeds in Sandia's Trisonic Wind Tunnel to ascertain the effects of Mach number and angle of attack on the interaction of a trailing vortex with a downstream control surface. Components of normal force, bending moment, and hinge moment were measured on an instrumented fin downstream of an identical fin at Mach numbers between 0.85 and 1.24, and combinations of angles of attack between -5º and 10º for both fins. The primary influence of upstream fin deflection is to shift the downstream fin's forces in a direction consistent with the vortex-induced angle of attack on the downstream fin. Secondary non-linear effects of vortex lift were found to increase the slopes of normal force and bending moment coefficients when plotted versus fin deflection angle. This phenomenon was dependent upon Mach number and the angles of attack of both fins. The hinge moment coefficient was also influenced by the vortex lift as the center of pressure was pushed aft with increased Mach number and total angle of attack.

1. Introduction

Maneuvering atmospheric flight vehicles often combine tail fins with upstream fins or canards for stability and control. On such vehicles, maneuverability may be attained through deflection of either the upstream or downstream fin, or a combination of both. On swept fins, when an upstream fin is deflected, leading edge separation forms a vortex that rolls up near the tip of the fin, contributing to the tip vortex, and proceeds downstream towards the trailing fin. This shed vortex may impinge upon the downstream fin, altering its aerodynamics. Correlations between Particle Image Velocimetry (PIV) and force balance data by Beresh et al.[1] suggest that the interaction is a result of an induced angle of attack on the downstream fin caused by the shed vortex from the upstream fin. A diagram of a representative finned body of revolution showing vortices shed from an upstream fin traveling towards a rear control surface is provided in Figure 1.

A previous study was performed in Ref. [2] in Sandia National Laboratories' Trisonic Wind Tunnel (TWT) on a subscale fin model to examine the effects of fin geometry, angle of attack, Reynolds number, and Mach number on the aforementioned vortex-fin interaction in subsonic flow. Two identical fins, separated axially by 4 root-chord lengths, were mounted on a solid wall of the TWT's test section and a three-component balance was utilized to measure the coefficients of normal force, bending moment, and hinge moment on the downstream fin. This effectively simulated a missile body at zero angle of attack, allowing a study of the aerodynamic interaction between the wake of the upstream fin and the downstream fin. The results from Mach 0.5 to 0.8 indicated that the primary influence of the upstream fin was to shift the trailing fin's forces dependent upon the upstream fin angle of attack. A

[1] Member of the Technical Staff, Engineering Sciences Center, Mailstop 0825, jussmit@sandia.gov; Member AIAA.
[2] Distinguished Technologist, Engineering Sciences Center, jfhenfl@sandia.gov; Member AIAA.
[3] Principal Member of the Technical Staff, Engineering Sciences Center, sjberes@sandia.gov; Senior Member AIAA.
[4] Distinguished Technologist, Engineering Sciences Center, twgrass@sandia.gov.
[5] Technologist, Engineering Sciences Center, rspille@sandia.gov.

This work is supported by Sandia National Laboratories and the United States Department of Energy. Sandia is a multiprogram laboratory operated by Sandia Corporation, a Lockheed Martin Company, for the United States Department of Energy's National Nuclear Security Administration under Contract DE-AC04-94AL85000.

secondary non-linear influence due to vortex lift, a suction force on the fin body induced by the vortex generated at the fin's leading edge,[3-7] was also identified in the subsonic data as it nonlinearly increased the slopes of normal force and bending moment coefficients and decreased the slope of the hinge moment coefficient as angle of attack was increased. Mach number was also shown to push the center of pressure aft, reducing the hinge moment coefficient at angles of attack above 5º. The only influence of Mach number on the force and moment coefficients was through its effects on vortex lift. Forces were also found to be relatively independent of fin planform area and Reynolds number when properly normalized.

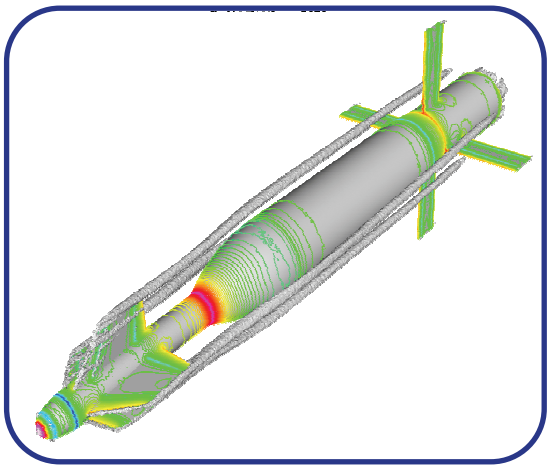

Figure 1. Vortices shed from an upstream fin interacting with trailing control surfaces.

The present study seeks to extend the previous subsonic vortex-fin interaction analysis to transonic Mach numbers. In this regime, predictive capabilities do exist but they often struggle to accurately predict the effects of the vortex-fin interaction on forces of downstream components. Slender body theory has been applied in many cases to predict the forces on fins from transonic to supersonic flow with and without the presence of interference from upstream components. Some good examples are given in Refs. [8-11]. Limited data are available on transonic flow of instrumented fins[12-13] and most open literature that consider forces on fins have little mention of the downstream influence from the wake of an upstream fin. Those reports that do discuss such an interaction are typically done using tandem delta wings with a fixed separation between the leading and trailing fin.[14-16] Higher fidelity analysis with CFD codes may provide more accurate solutions, but they must ultimately be validated with experimental data.

In this study, forces and moments were measured on a single subscale fin geometry in order to investigate the vortex-fin interaction, to supply data for CFD code validation, and to provide a database to aid in future vehicle design. Multiple combinations of flow conditions and angles of attack between -5° and 10° were examined. This paper describes the balance system, experimental setup, and force measurement results on single fins and in an interaction between the shed vortex of an upstream and a downstream fin from Machs 0.8 to 1.2.

2. Experimental Apparatus

Trisonic Wind Tunnel

Experiments were performed in Sandia's Trisonic Wind Tunnel (TWT), which is a blowdown-to-atmosphere facility using air as the test gas through a 305 x 305 mm^2 (12 x 12 in^2) rectangular test section enclosed within a pressurized plenum. The TWT is capable of running at Mach Numbers from 0.5 to 3.0 and unit Reynolds Numbers from 10 to 60 million/m (3 to 18 million/ft). Typical run times are from 20-120 seconds with a turnaround time of 20-30 minutes.

Previous vortex-fin studies have used a solid-wall transonic test section for analyses from Mach 0.5 to 0.8. A half-body configuration, in which three of the tunnel's four walls are porous, was employed for the current analysis to alleviate the problem of transonic choking near Mach 1 and to prevent the reflection of normal shock waves back onto the test body. The remaining wall was kept solid to represent a simplified missile body. A photograph of the TWT in the half-body configuration with an attached fin is provided in Figure 2. In this photo the flow path is from right to left.

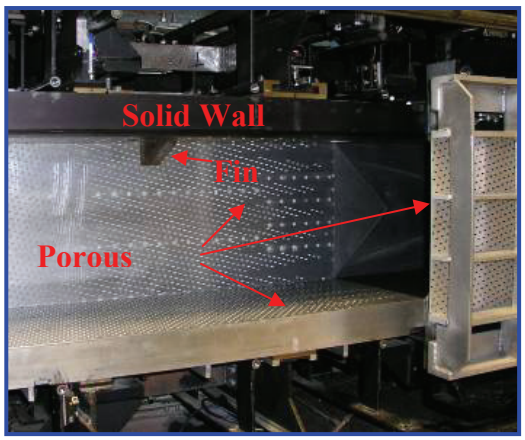

Figure 2. Picture of the Trisonic Wind Tunnel showing the half-body configuration (3 porous and 1 solid wall) with attached fin.

Fin Force Balance and Attachment Hardware

The fin geometry and balance system are described in detail in Ref. [2]. In that study, several geometries were investigated at subsonic speeds up to Mach 0.8. Characteristics common to all of those geometries include a trapezoidal planform, 45º leading edge sweep, no trailing edge sweep, aspect ratio of 2/3, and a sharp leading edge with a taper that terminates at a distance x from the leading edge, after which a constant thickness is maintained. The baseline fin geometry had a 76.2 mm (3 in) root chord, 38.1 mm (1.5 in) span, 3.18 mm (0.125 in) thickness, and x varying linearly over the fin's span so as to maintain a constant ratio of 1/3 of the local chord. In addition to the baseline fin, two scaled-up versions with root-chords of 101.6 mm (4 in) and 152.4 mm (6 in), a variant with twice the thickness, and a variant with a constant x of 25.4 mm (1in) were also tested. Since the force and moment results of the previous study were found to be relatively independent of the geometric variations described above, only the baseline fin was used for the current study. A diagram of the baseline fin is displayed in Figure 3. Here, dimensions are in mm.

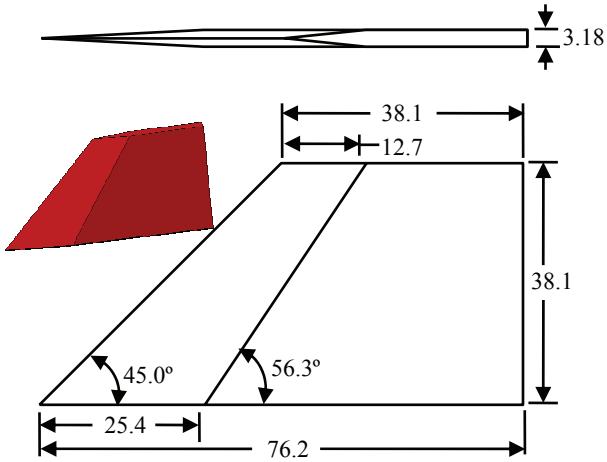

Figure 3. Baseline fin geometry. Dimensions in mm.

The baseline fin was attached to a three-component (normal force, bending moment, and hinge moment) force balance supplied by Allied Aerospace's Force Measurement Systems division. Fins attach to the balance through the top solid wall within the test section via a cylindrical adaptor hub such that the fin resides within the test section, at a 1.5 mm (0.06 in) gap from the wall, and the balance sits on the outside of the test section. The cylindrical hub allows for the angle of attack of the fin to be changed by rotating the fin along with the entire balance system. Since the fin and balance are rotated together, the measured force components are always in the local fin body coordinate system, and no coordinate transformation is needed. Additionally, this allows for the fin angle setting mechanism to be located at the top of the balance canister and out of the tunnel. The system allows for very precise and repeatable angle settings from -5º to 10º in 1º increments. A diagram displaying the fin-balance attachment mechanism is provided in Figure 4.

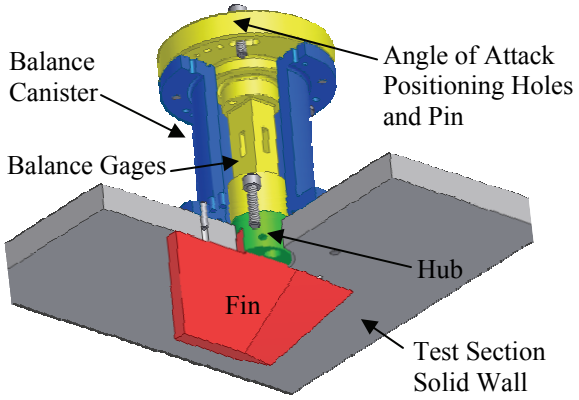

Figure 4. Fin balance cutout showing fin attachment.

The fin axial position is set using sliding insert plates on a rail cut into the test section top wall. This allows the whole system, balance and all, to be moved upstream or downstream as needed for multi-fin studies. The inserts are composed of aluminum and black anodized to reduce background light scatter during PIV studies. For cases with both upstream and downstream fins, the upstream fin is not instrumented and instead has a lower profile dummy balance system attached. On the dummy balance, the upstream fin's angle of attack and axial position is adjusted in the same manner as the downstream instrumented fin. Because of the smaller stature of the dummy balance, limitations placed upon the instrumented fin because of a lack of clearance in places above the test section are not imposed upon the upstream fin. Thus, it may be positioned anywhere within the 457 mm (18.0 in) traversing length of the rail.

Because of clearance issues above the test section wall, all measurements in the current analysis had the instrumented fin fixed at 508 mm (20 in) downstream of the contraction. Thus, for two-fin cases, the upstream fin was moved when the spacing of the fins needed to be changed.

The majority of data were acquired with the same balance used in the previous subsonic study, the 50 lb-balance. This balance is capable of maximum loads of 222 N (50 lb) normal force, 7.0 N-m (62.4 in-lb) root bending

moment, and 3.0 N-m (26.2 in-lb) hinge moment with uncertainty levels from 0.1 to 0.2% full-scale in each of the components. This balance allows for more precise measurements at low force levels than the larger balance, which was used in this study to make measurements at force levels that would saturate the smaller balance. The 200 lb-balance system is capable of acquiring data for normal force, bending moment, and hinge moment, with maximum loads of 888 N, 28.2 N-m, and 12.7 N-m (200 lbs., 250 in-lbs., and 112 in-lbs), respectively. Calibration uncertainties for the larger balance were also between 0.1 and 0.2% of the full-scale force values. These, and the smaller balance's, uncertainty values were calculated at the 95% confidence level from the standard deviations of the manufacturer's linear calibration fitting errors. The load ranges of these two balances were designed using an Air Force correlation-based missile design code, Missile Datcom,[17] and an Euler CFD code, Splitflow,[18] for single and aligned fins at the test freestream conditions.

Check loads were applied to the balance by adapting it to Sandia's calibration stand, normally used for calibrating internal balances, and replacing the fin with a calibration plate. The plate had eighteen total weight-hanging locations, three each for hinge and bending moment loading and roll settings of 0º and 180º. The combination of different loading positions and weight magnitudes allow loading of all three components simultaneously and thus excite interactions between them, allowing a full calibration on a 3 × 9 matrix. A picture of the calibration stand is presented in Figure 5.

Figure 5. Sandia's balance calibration stand.

A series of check loads were applied to the balance while on the calibration stand to verify that the manufacturer's calibration matrix was valid. When reduced, these independent loads were all within the manufacturer's uncertainty levels, so the manufacturer's calibration was deemed adequate and was used to reduce all subsequent test data.

Calibration shunt resistors were applied to simulate a load to the balance once it was placed into the tunnel. The output with this simulated load was compared to the same output when the balance was on the calibration stand to ensure that there was no difference in the instrumentation that would alter the balance output.

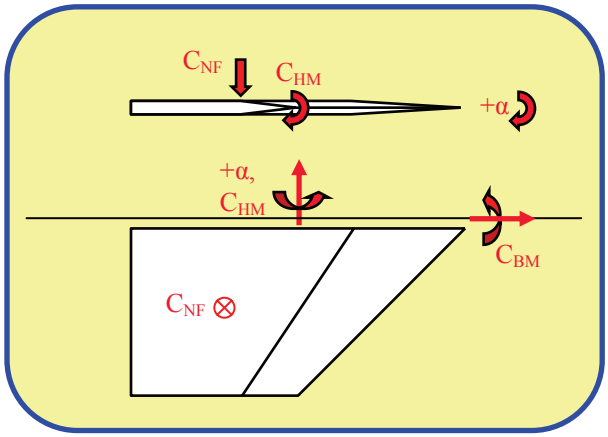

Figure 6. Force diagram of a fin as it sits on the top wall of the TWT. Flow is from right to left.

A force and moment diagram depicting the fin as it resides on the tunnel top wall is provided in Figure 6. Here, flow is from right to left. Forces and moments are presented in coefficient form, normalized by the local freestream dynamic pressure measured at the same axial position as the instrumented fin, q_2, the fin planform area, S, and bending moment and hinge moment reference lengths, l_b and l_h. For the baseline fin, S = 2117.4 mm^2 (3.375 in^2), l_b = 38.1 mm (1.5 in), and l_h = 57.2 mm (2.25 in). The normal force coefficient, C_{NF} = NF/q_2S, was defined to be positive into the page when acting on a fin oriented as in Figure 5. The bending moment coefficient, $C_{BM} = BM/q_2Sl_b$, is referenced about the tunnel wall and a positive moment would tend to roll the fin tip into the page. The hinge moment coefficient, $C_{HM} = HM/q_2Sl_h$, is referenced about the fin's root half-chord, and positive moment would roll the fin's leading edge into the page and its trailing edge out of the page.

In addition to force and moment measurements, the center of pressure of the fin is reported for each of the runs. The chordwise location of center of pressure, x_{cp}, is calculated from the ratio of hinge moment to normal force, x_{cp} = HM/NF, while the spanwise component, y_{cp}, is calculated from the ratio of bending moment to normal force, y_{cp} = BM/NF. Thus, x_{cp} is referenced at the fin root half-chord and increases towards the leading edge of the fin. The spanwise center of pressure is referenced at the tunnel wall and increases towards the fin's tip.

Experimental Conditions

The experimental conditions for previous subsonic studies using the solid wall test section were determined by two static pressure taps on the test section side wall. The upstream pressure tap was located at the beginning of the test section, x = 0 in, and was used to set the nominal freestream conditions ahead of the two fins. The second tap was located at the position of the downstream instrumented fin at x = 20 in. This provided a direct measurement of the freestream conditions at the downstream fin location, and because the taps were on the sidewall, interference due to the presence of the fins was negligible. Boundary layer growth within the constant-area duct of the solid-wall test section causes a rise in Mach number with downstream distance. Typical variations of a few percent, depending on the set Mach number, were seen between measurements at x = 0 and x = 20 in.

Boundary layer growth on the solid wall of the half-body configuration does not result in the same Mach number increase seen in the solid wall test section because outflow at the porous walls allows expansion of the gas, which compensates for boundary layer effects. However, above Mach 1, an axial variation in Mach number is seen in tunnels such as the TWT, which uses a sonic nozzle and porous walls enclosed within a passive plenum chamber in order to establish supersonic flow.[19] Above Mach 1, the porous walls allow streamlines within the test section to diverge, creating a virtual converging-diverging nozzle that further expands the flow to the desired operating Mach number. Thus, a considerable Mach gradient exists at the beginning of the test section where this expansion occurs.

The porous sidewalls of the half-body configuration preclude the use of side-wall pressure taps, so static pressure measurements had to be taken on the top solid wall. For this task, pressure taps were drilled into a top wall insert plate at 18 axial locations extending from x = 4.125 in to x = 21.125 in at 1-in intervals. All taps were located 3.0 in off tunnel centerline and had a diameter of 0.032 in.

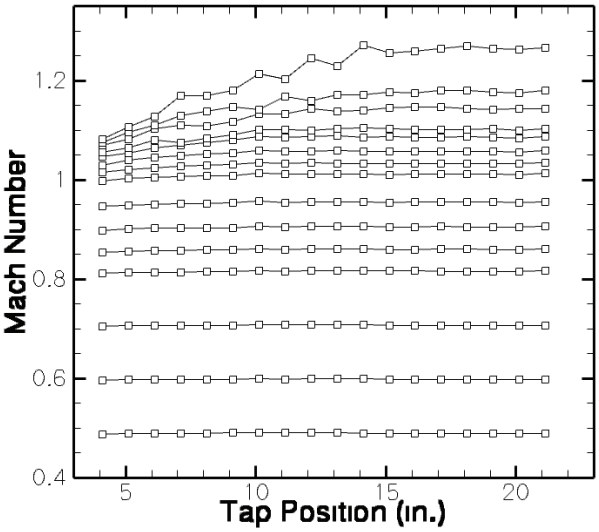

Figure 7. Mach number vs. axial distance in the TWT.

Empty tunnel runs were made to establish the extent of the variation in Mach number with axial position due to the expansion phenomenon described above. Mach numbers are plotted in Figure 7 vs. axial distance within the test section. This figure shows the variation in Mach number within the test section for various run conditions encompassing those studied in this and the previous analysis. Here, the variation is seen to be relatively small for low Mach numbers but increases for conditions above Mach 1. The largest variation is seen for the Mach 1.27 case, where the greatest expansion occurs. Here Mach number varies from 1.08 at tap location 1 to 1.27 at x = 20 in. Thus, for cases with two fins, particularly at higher Mach numbers, the shed vortex forms under different conditions from those seen by the downstream fin.

Top wall pressure taps are advantageous because they provide a global picture of the freestream conditions that a shed vortex encounters as it travels downstream towards the rear fin. However, due to their close proximity to the fins, they are also susceptible to fin wake interference. An example illustrating this interference is provided in Figure 8, where static pressure ratio is plotted vs. axial location for several cases of upstream fin angle of attack. In all cases, the fin was located at x = 8 in and the nominal Mach number was 1.05. In the figure, p_1 is the pressure at tap location 1, x = 4.125 in.

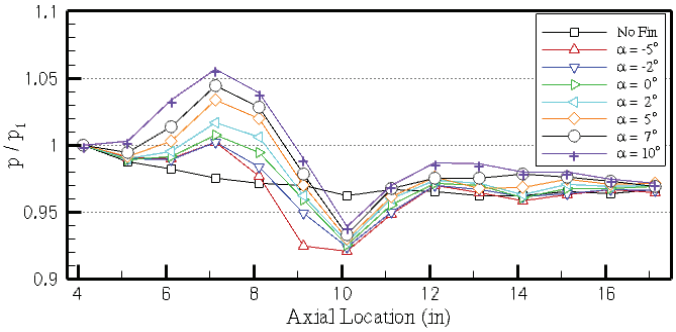

Figure 8. Influence of fin wake on static pressure ratio.

Figure 8 illustrates that the interference extends about one fin length upstream and two fin lengths downstream at the spanwise location of the pressure taps. Thus, due to this interference, the pressure tap measurements taken during a test do not accurately depict freestream conditions in the tunnel. To alleviate this problem, a correlation

was developed to relate the Mach number and pressure ratio measured at tap location one, M_1 and p_1/p_0, which remain virtually unaffected by the presence of the downstream fins, to those values at several downstream locations, M_x and p_x/p_0. Empty tunnel data were taken encompassing the range of subsonic to transonic tunnel conditions examined in this and the previous fin study (roughly Mach 0.5 to 1.27). The data, which are presented in Figure 9, collapsed to a single line for each axial location and were fitted with a shape-preserving piecewise cubic spline. The variations in the data with axial location seen above Mach 1 are a result of the expansion referred to previously. The estimated error in the fit is 0.001 to 0.003, depending on axial location, in both Mach and pressure ratio.

Instrumented fins were tested at freestream Mach numbers of M = 0.85, 0.91, 0.96, 1.01, 1.06, 1.11, and 1.24. These values were determined at the fin center from pressure tap data at location 1 and the correlations presented in Figure 9. Corresponding static pressures at x = 20 in, stagnation pressures and temperatures, and unit Reynolds numbers are provided in Table 1. It should be noted here that the differences in Reynolds numbers seen in Table 1 are not expected to affect the results of this analysis as a Reynolds number study was performed in the previous analysis and, to within the measurement uncertainty, the forces were found to be independent of Reynolds number.

For all measurements, the instrumented fin was located 20 inches downstream of the contraction, i.e. 20 inches from the beginning of the test section. Thus, for a particular set of tunnel conditions, the fin always saw the same boundary layer. Boundary layer profiles extracted from PIV measurements and other tunnel properties have been examined for the TWT in the solid-wall configuration and reported by Beresh, et al.[20] In that paper, the boundary layer thickness was found to range from 14.5 mm (0.57 inches) at Mach 0.5 to 13.5 mm (0.53 inches) at Mach 0.8 under tunnel operating conditions similar to those reported in Table 1. As of yet, no experimental boundary layer data has been obtained for the half-body configuration at higher Mach numbers, but such measurements are planned for the near future.

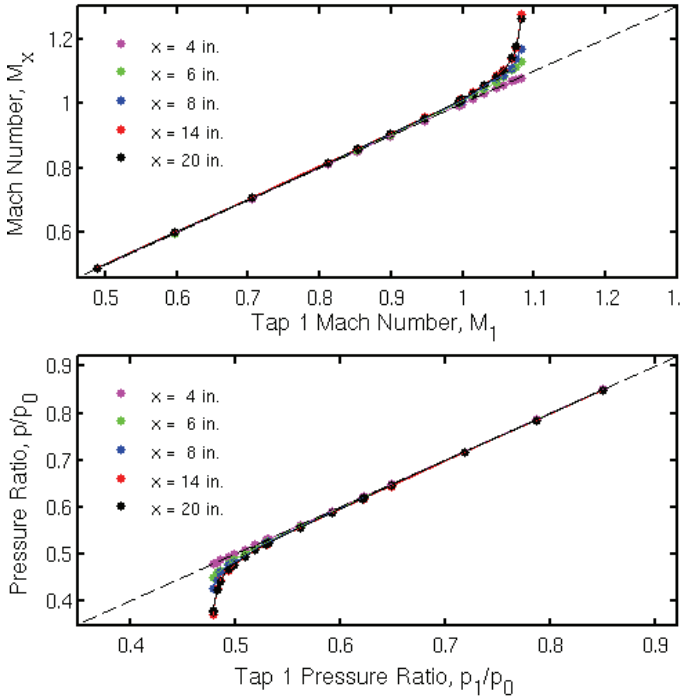

Figure 9. Correlation of freestream conditions at pressure tap 1 to conditions at several downstream locations. (a) Ratio of static pressure to stagnation pressure. (b) Mach number.

Table 1. Experimental Conditions.

$M_{x=4.125"}$	$M_{x=20"}$	P_0, kPa	P_∞, kPa	T_0, K	Re, m^{-1}
0.50	0.52	121	102	325	11×10^6
0.60	0.61	130	102	325	13×10^6
0.70	0.72	142	102	325	16×10^6
0.80	0.84	156	102	325	22×10^6
0.83	0.85	155	97	326	19×10^6
0.90	0.91	171	101	325	22×10^6
0.95	0.96	180	100	325	23×10^6
1.00	1.01	190	100	325	25×10^6
1.03	1.06	203	100	325	27×10^6
1.06	1.11	216	99	326	29×10^6
1.08	1.24	244	99	326	31×10^6

3. Uncertainty Analysis

Data uncertainties (U) exist in this system as both systematic, or bias errors (B); and random, or precision errors (P). Possible sources of error include, but are not limited to, flow condition bias and repeatability, strain gage temperature and electronics effects, calibration bias and precision errors, and hardware related errors such as fin angle and axial location bias and repeatability. Care has been taken to eliminate the bias errors as much as possible; for example, the strain gage readings were temperature compensated and fin angles were set with a tightly toleranced pin to provide accurate and repeatable angle settings.

In the previous study, the measurement uncertainty was calculated from several repeat runs taken over the course of testing and was found to be on the same order as the calibration uncertainty. Repeat runs performed during the current analysis have confirmed the same behavior, with the calculated measurement uncertainty being nearly identical to the calibration uncertainty values. Thus, using the manufacturer's calibration uncertainty values for each balance, the measurement uncertainty of the force and moment coefficients may be calculated as described in the following paragraphs.

The uncertainties in the force and moment coefficients, assuming negligible contribution from variations in geometry, are given by

$$U_{C_{NF}}^{\ 2} = C_{NF}^{\ 2}\left(\frac{U_{NF}^{\ 2}}{NF^2} + \frac{U_q^{\ 2}}{q^2}\right), \quad U_{C_{BM}}^{\ 2} = C_{BM}^{\ 2}\left(\frac{U_{BM}^{\ 2}}{BM^2} + \frac{U_q^{\ 2}}{q^2}\right), \quad U_{C_{HM}}^{\ 2} = C_{HM}^{\ 2}\left(\frac{U_{HM}^{\ 2}}{HM^2} + \frac{U_q^{\ 2}}{q^2}\right). \tag{1}$$

Dynamic pressure is calculated using the correlations of pressure and Mach number of Figure 9 and the equation: $q = 1/2\gamma p M^2$. Thus, the uncertainty in dynamic pressure is given by

$$U_q^{\ 2} = q^2\left(2\frac{U_M^{\ 2}}{M^2} + \frac{U_p^{\ 2}}{p^2}\right) \tag{2}$$

The uncertainties in Mach number and pressure are a root-sum-square combination of the precision and bias uncertainties in the measurement of each quantity and in their propagation through the empty tunnel correlations. These combine to give typical values of 0.01 in Mach number uncertainty and 0.1 psi in static pressure uncertainty. These values are then propagated back through Equations 1 and 2 for each run to calculate the uncertainties in the force and moment coefficients. A typical run at Mach 1.11 had $U_q = 0.2$, $U_{CNF} = 0.01$, $U_{CBM} = 0.007$, and $U_{CHM} = 0.002$.

4. Results

Single Fin Results

The coefficients of normal force, bending moment, and hinge moment of a single fin are displayed for all Mach numbers in Figure 10. All three components exhibit the same trends as the subsonic data presented previously. For C_{NF} and C_{BM}, the data are linear at moderate angles of attack but their slopes increase at angles above 5º due to vortex lift. This effect is increased as stronger vortices are generated at higher angles of attack and Mach numbers up to 1. Above Mach 1, the coefficients begin to fall, particularly at higher angles of attack. This effect is more easily seen in Figure 11, where the force and moment coefficients are plotted vs. Mach number. Subsonic data from the previous study are also included to provide an indication of the Mach number effect in the subsonic range up to Mach 0.8. The discontinuity in the data near Mach 0.8 results from the slightly different conditions experienced in the TWT between the solid-wall and half-body test section.

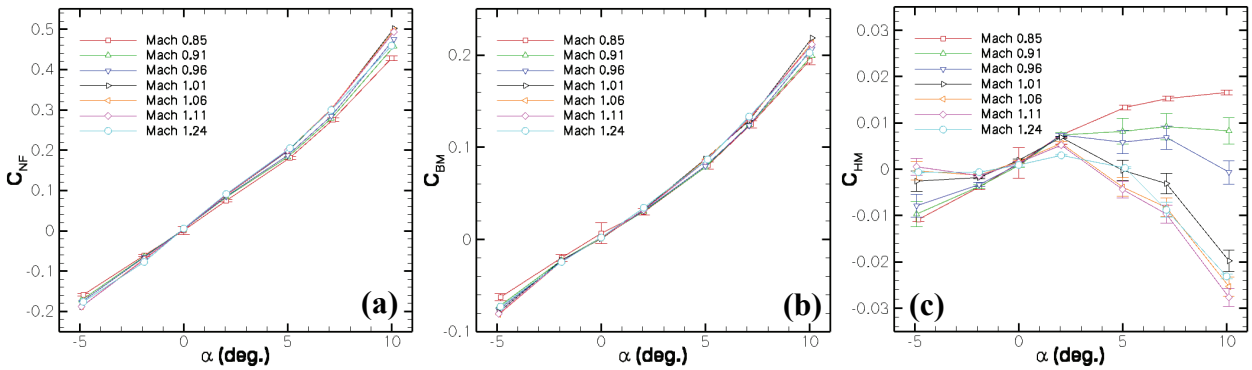

Figure 10. Force and moment coefficients vs. angle of attack. (a) C_{NF}, (b) C_{BM}, (c) C_{HM}.

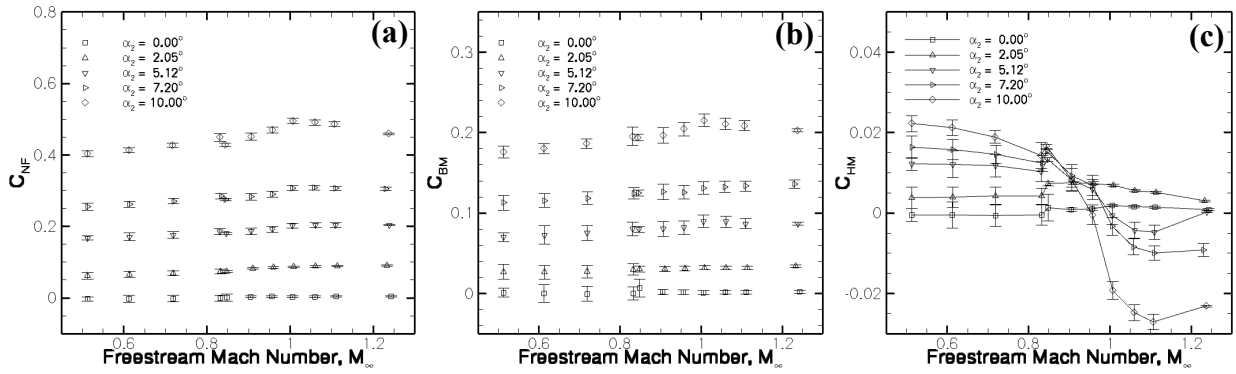

Figure 11. Force and moment coefficients vs. Mach number. (a) C_{NF}, (b) C_{BM}, (c) C_{HM}.

The same behavior as seen in Figures 10 and 11 was reported by Polhamus[3], who used a leading edge suction analogy to predict forces on delta wings. This suction analogy was extended to cropped delta wings by Lamar[4]. Both papers predicted decreased vortex lift above Mach 1, and experimental data for delta wings produced by Squire et al.[21] and reproduced in Polhamus' paper also indicated a decrease in the size of the leading edge vortex and in the magnitude of the vortex lift above Mach 1.

At Mach 0.85, the hinge moment coefficient increases with angle of attack, but as Mach number is increased, the coefficient begins to fall with increasing α, even crossing zero at cases above Mach 1. Since the normal force coefficient is positive and increasing over the entire angle of attack range, this indicates that the center of pressure is being pushed back behind the center of the fin.

The effect of Mach number and angle of attack on center of pressure is presented in Figure 12. Here, centers of pressure are shown with respect to their position on the fin for each Mach number tested. The predominant direction of variations due to angle of attack is specified by arrows in the figure. Typical measurement uncertainties correspond to 0.02 inches in x_{cp} and 0.04 inches in y_{cp}. Comparatively, the data vary by about 0.4 inches in x_{cp} and 0.2 inches in y_{cp}. The data indicate that the center of pressure is pushed aft and out at higher Mach numbers and angles of attack, and the increased spread in the data suggests that the effect of angle of attack is stronger at higher Mach numbers. The trends are a result of the increased vortex lift with Mach number (up to Mach 1) and angle of attack. As angle of attack and Mach number are increased, the size of the leading edge vortex increases. The increased suction force acting over a larger area on the leeward side of the fin increases the normal force and bending moment coefficients. The hinge moment coefficient decreases and center of pressure moves aft as vortex size increases near the fin tip, which lies behind the moment reference point. The center of pressure also moves toward the tip because of this increased vortex size near the fin tip.

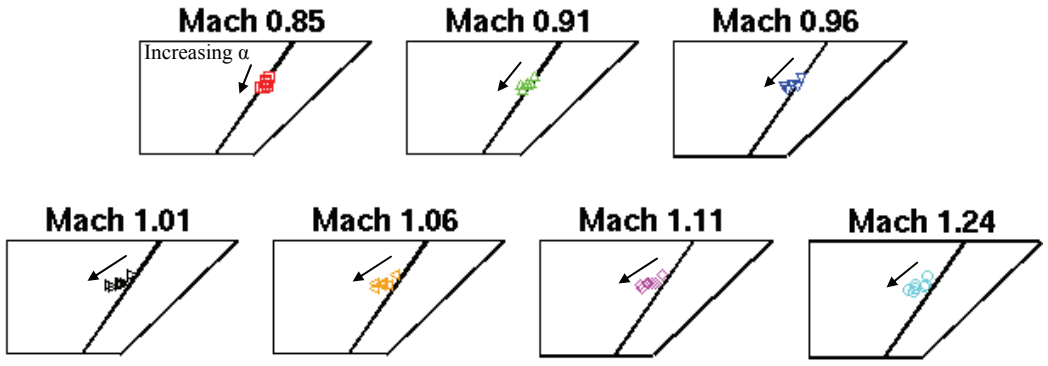

Figure 12. Effect of Mach number and angle of attack on center of pressure. The direction that center of pressure moves with increasing α is specified by the arrows.

Two Fin Results

Two-fin data are presented in Figure 13 for the case of a fin at a distance of 4 root chord lengths (305 mm) downstream of an identical fin, measured from fin center to fin center. In the figure, the downstream fin's force and moment coefficients are plotted as a function of its angle of attack, α_2, with separate curves drawn for each upstream fin angle, α_1, and Mach number combination. For comparison, the single fin data at Mach 0.85 are also included as black triangles. As seen previously in the subsonic data and discussed in Ref. [1], the primary influence of the upstream fin is to induce an angle of attack on the downstream fin, shifting its normal force and bending moment coefficients with the strength of the shed vortex. The magnitudes of C_{NF} and C_{BM} increase with Mach number up to 1, and then decrease slightly with Mach number above the sonic case. This is the same non-linear behavior caused by vortex lift that was revealed in Figure 10 for the single fin case, but with two fins, the correlation must be made to the total angle of attack on the fin, α_{total}, which is a combination of the trailing fin's physical angle, α_2, and the vortex-induced angle of attack, $\alpha_{induced}$. The magnitude of the vortex lift is seen to increase with the total angle of attack. For cases when $\alpha_{induced}$ is in the same direction as α_2, i.e. when the two fins are deflected in opposite directions, α_{total} is increased, and the vortex lift is enhanced. For cases when the upstream and downstream fins are deflected in the same direction, $\alpha_{induced}$ and α_2 have opposite signs, resulting in decreased vortex lift.

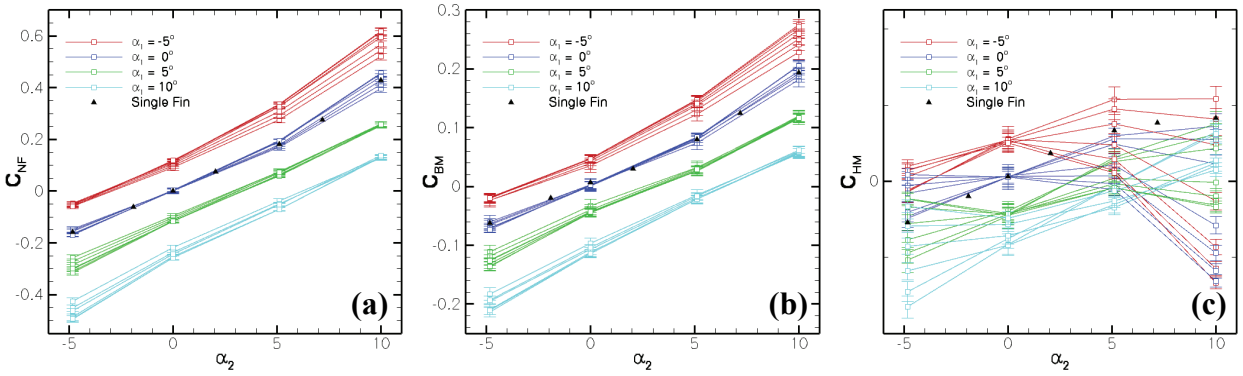

Figure 13. Aerodynamic coefficients vs. angle of attack of a baseline fin four root chord lengths downstream of another baseline fin. (a) C_{NF}, (b) C_{BM}, (c) C_{HM}. Single fin forces at Mach 0.85 are included for comparison.

The hinge moment coefficients of Figure 13(c) were purposefully plotted together to show their strong dependence on both Mach number and angle of attack. Considered separately, the upstream angle of attack shifts this component in the same manner as the normal force and bending moment components. Mach number influences the hinge moment coefficient by pushing the center of pressure aft on the fin, thus decreasing C_{HM} with respect to Mach at a constant α_2 when C_{NF} is positive and increasing C_{HM} with respect to Mach for negative C_{NF}. This behavior is consistent with the single fin results.

The aerodynamic coefficients are plotted vs. Mach number in Figure 14, where the subplots are arranged in 3 columns, 1 each for the 3 force and moment components. Within these columns, the subplots on each row correspond to downstream fin angle, and the individual lines within each plot represent upstream fin angle. Discontinuities in the data near Mach 0.8 are again attributed to slight differences in tunnel conditions between the solid-wall and porous-wall half-body configurations used in this and the previous subsonic analysis. The data illustrate the effects of Mach number on vortex lift, highlighted in the increased magnitudes of normal force and bending moment coefficients up to Mach 1 and the subsequent decreases in these components above Mach 1, as was seen previously for the single fin case.

The hinge moment data show the same trends with Mach number noted previously in the discussion of Figure 13. The primary influence of Mach number is to push the center of pressure aft on the downstream fin. The secondary effect of increased (or reduced) vortex lift, depending on the sign of α_{total}, is noticed when looking at the individual plots (a single α_2 case). For example, the case of α_2 = 10º (the bottom, right plot) shows a reduced dependence of C_{HM} on Mach number as α_1 goes from -5º to 10º. This suggests that the magnitudes of α_2 and $\alpha_{induced}$ are converging, canceling one another.

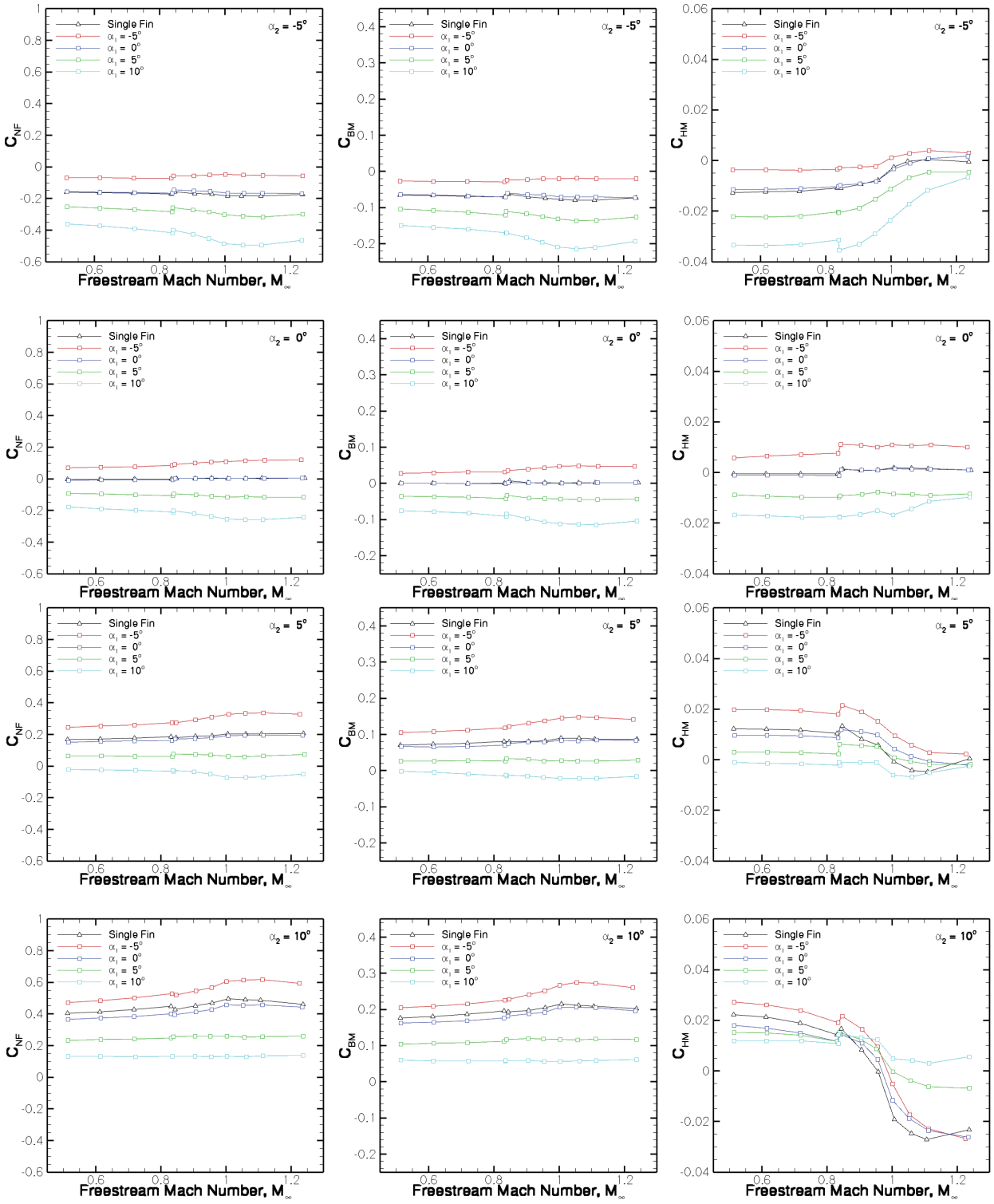

Figure 14. Aerodynamic force and moment coefficients vs. Mach number for two aligned fins separated by 4 fin root chords.

Finally, the effects of Mach number, upstream fin angle, and downstream fin angle on center of pressure may be deduced from the center of pressure plots displayed in Figure 15 in conjunction with the force plots of the previous two figures. Uncertainties in the measurement of x_{cp} and y_{cp} are of the same order of magnitude as for the single fin case near 0.02 and 0.04 inches, although cases where $C_{NF} \approx 0$ produce much larger uncertainties. This is a common problem in center of pressure calculations, for which the usual remedy is to use derivatives near $C_{NF} = 0$ to reduce the error. In this case, the data are so sparse (5º-increments in α_2) that they are not linear between points and accurate derivatives cannot be calculated.

In Figure 15, data are arranged into separate plots for each Mach number, and the four distinct upstream fin angles of attack are distinguished on each plot by the four symbols shown in the legend. For clarity, only the $\alpha_2 = 10º$ case is shown.

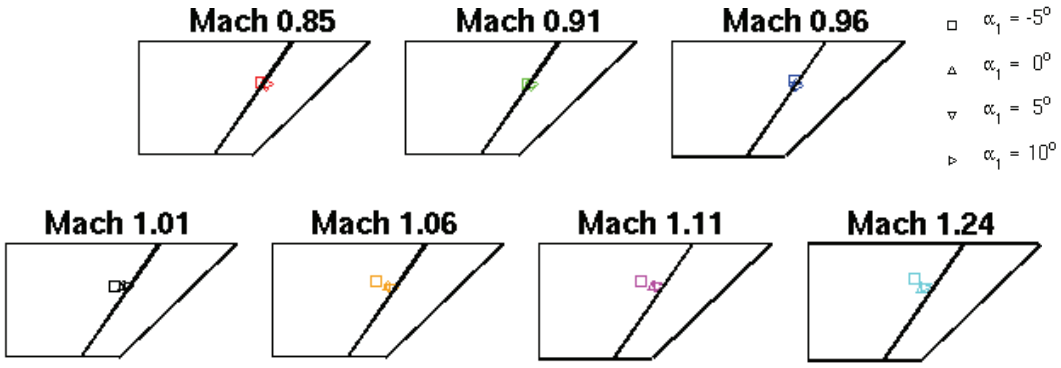

Figure 15. Effect of Mach number and angle of attack on center of pressure of a cropped delta wing 4 root chord lengths downstream of an identical upstream fin. Upstream angle of attack values are defined in the legend while the downstream angle of attack was 10º in all cases.

The chordwise component, x_{cp}, was seen in the single fin data to move aft with increasing angle of attack. With two fins, the combination of angles of attack of both fins and Mach number must be considered. The available data suggest that for all combinations of upstream and downstream fin deflection, increasing Mach number up to 1 has the effect of pushing x_{cp} aft on the fin. Above Mach 1, x_{cp} is expected to move forward, as was seen in the single fin case, but uncertainties in the data prevent that determination from being made. The data also suggest that x_{cp} moves aft as the magnitude of α_{total} increases, this would correspond to decreasing α_1 in the figure. The spanwise component, y_{cp}, is relatively independent of angle of attack and Mach number. This differs from the behavior seen in the single fin data, and is somewhat counter-intuitive as an increased y_{cp} is expected with α_{total}. Nevertheless, that effect is not seen, possibly due to spanwise motion from the impinging vortex. The data for the other three angle of attack cases exhibit similar trends.

5. Conclusions and Future Work

Maneuvering atmospheric flight vehicles often combine tail fins with upstream fins or canards for stability and control. On swept fins, when an upstream fin is deflected, leading edge separation and subsequent reattachment forms a vortex that rolls up near the tip of the fin, contributes to the formation of the tip vortex, and proceeds downstream towards the trailing fin. The shed vortex may then impinge upon a downstream fin, inducing an angle of attack and altering its aerodynamics. Current predictive capability based on correlations and slender body theory is lacking in the transonic regime, as non-linear effects due to vortex lift are not well-demonstrated. Higher fidelity simulations with CFD codes may provide more accurate solutions, but they must ultimately be validated with experimental data. Knowledge of the vortex-fin interaction through experiments is thus needed for code and model validation and for the successful design of fins and control algorithms on these types of vehicles.

Force and moment measurements have been made on an instrumented subscale fin model at transonic speeds to ascertain the aerodynamic effects of the vortex-fin interaction. Components of normal force, bending moment, and hinge moment were measured on an instrumented fin downstream of an identical fin at Mach numbers between 0.85 and 1.24, and combinations of angles of attack between -5º and 10º for both fins. Data were also acquired for the case of no upstream fin to establish a baseline for comparison to the two-fin data.

Single fin force coefficients are linear at moderate angles of attack, but exhibit non-linear behavior due to vortex lift above $\alpha = 5º$, where the slopes of C_{NF} and C_{BM} are increased and C_{HM} is decreased. The center of pressure is also

pushed aft and out due to vortex lift as suction forces on the leeward side result in greater pressure differential at the tip and aft portions of the fin. The effects of vortex lift grew as Mach number (up to 1) and angle of attack were increased as greater suction forces acting over a larger area on the leeward side of the fin were produced.

In two-fin data, the primary influence of upstream fin deflection is to shift the downstream fin's forces dependent upon the upstream angle of attack. The same non-linear vortex lift trends of the single fin data were also present in the two-fin data when comparing the total angle of attack, physical plus vortex-induced, to the two-fin force and moment coefficients. This supports the proposition that the upstream shed vortex induces an angle of attack on the downstream fin, which adds to the angle of attack seen by the fin. A notable exception is that y_{cp} does not seem to move outward with increased total angle of attack for the two-fin data, whereas it did in the single-fin data. The reason for this is still unresolved.

PIV data near the fin leading edge are currently being analyzed and may provide insight into why the vortex lift is dependent on Mach number when the downstream measurements suggest that normalized strength of shed vortices are independent of Mach number. These data may also resolve the mechanism of the trends seen in center of pressure as Mach number and angle of attack were varied. Pressure Sensitive Paint (PSP) will be applied on a fin to determine the pressure and force distribution on a downstream fin during subsonic vortex-fin interactions. Finally, further PIV and force and moment studies are also planned with a simulated missile body angle of attack to determine its effects on the interaction.

Acknowledgements

The authors would like to thank the following Sandia National Laboratories staff members for their support of the present work: W. P. Wolfe, R. B. Bond, and C. W. S. Bruner.

References

[1]Beresh, S. J., Smith, J. A., Henfling, J. F., Grasser, T. W., and Spillers, R. W., "Interaction of a Fin Trailing Vortex with a Downstream Control Surface," AIAA Paper 2008-0342, Jan. 2008

[2]Smith, J. A., Henfling, J. F., Beresh, S. J., Grasser, T. W., and Spillers, R. W., "A Three-Component Balance System for Measuring Forces and Moments in Fin-Wake Interactions," AIAA Paper 2007-5319, July 2007.

[3]Polhamus, E. C., "Predictions of Vortex-Lift Characteristics by a Leading-Edge Suction Analogy," Journal of Aircraft, Vol. 8, No. 4, 1971, pp. 193-199.

[4]Lamar, J. E., "Prediction of Vortex Flow Characteristics of Wings at Subsonic and Supersonic Speeds," Journal of Aircraft, Vol. 13, No. 7, 1976, pp. 490-494.

[5]Purvis, J. W., "Analytical Prediction of Vortex Lift," AIAA Paper 1979-0363, Jan. 1979.

[6]Dodbele, S. S. and Plotkin, A., "Prediction of Vortex Lift on Interacting Delta Wings in Incompressible Flow," Journal of Aircraft, Vol. 21, No. 7, 1984, pp. 451-452.

[7]Hemsch, M. J. and Luckring, J. M., "Connection between Leading-Edge Sweep, Vortex Lift, and Vortex Strength for Delta Wings," Journal of Aircraft, Vol. 27, No. 5, 1990, pp. 473-475.

[8]Oberkampf, W. L., "Prediction of Forces and Moments on Finned Missiles in Subsonic Flow," AIAA Paper 79-0365, Jan. 1979.

[9]Oberkampf, W. L. and Nicolaides, J. D., "Aerodynamics of Finned Missiles at High Angle of Attack," AIAA Paper 1971-50, Jan. 1971.

[10]Oberkampf, W. L., "Prediction of Forces and Moments on Finned Bodies at High Angle of Attack in Transonic Flow," Sandia National Lab., SAND80-2380, Albuquerque, NM, April 1981.

[11]Hemsch, M. J., Nielsen, J. N., Smich, C. A., and Perkins, S. C., "Component Aerodynamic Characteristics of Banked Cruciform Missiles with Arbitrary Control Deflections," AIAA Paper 77-1153, Aug. 1977, pp. 288-299.

[12]Allen, C. Q., Schwind, R. G., and Malcolm, G. N., "Canard-Body-Tail Missile Test at Angles of Attack to 50^{o} in the Ames 11-Foot Transonic Wind Tunnel," NASA-TM-78441, Sept. 1978.

[13]Hemsch, M. J., Nielsen, J. N., "The Equivalent Angle-of-Attack Method for Estimating the Nonlinear Aerodynamic Characteristics of Missile Wings and Control Surfaces," AIAA Paper 1982-1338, August 1982.

[14]Erickson, G. E., Schreiner, J. A., and Rogers, L. W., "Canard-Wing Vortex Interactions at Subsonic Through Supersonic Speeds," AIAA Paper 1990-2814, Aug. 1990.

[15]Erickson, G. E., Schreiner, J. A., and Rogers, L. W., "On the Structure, Interaction, and Breakdown Characteristics of Slender Wing Vortices at Subsonic, Transonic, and Supersonic Speeds," AIAA Paper 89-3345, Aug. 1989.

[16]Bergmann, A. and Hummel, D., "Aerodynamic Effects of Canard Position on a Wing Body Configuration in Symmetrical Flow," AIAA Paper 2001-0116, Jan. 2001.

[17]Blake, W. B., "Missile DATCOM: User's Manual – 1997 Fortran 90 Revision," U.S. Air Force Research Lab/Air Vehicles Directorate, Wright-Patterson Air Force Base, OH, 1998.

[18]Karman, S. L., "SPLITFLOW: A 3D Unstructured Cartesian/Prismatic Grid CFD Code for Complex Geometries," AIAA-95-03436.

[19]Goethert, B. H., "Transonic Wind Tunnel Testing," Dover Publications, Inc., Mineola, NY, 2007.

[20]Beresh, S. J., Henfling, J. F., Spillers, R. W., and Erven, R. J., "Measurement of Experimental Boundary Conditions for CFD Validation of a Supersonic Jet in Transonic Crossflow," AIAA Paper 2006-3449, June 2006.

[21] Squire, L. C., Jones, J. G., and Stanbrook, A., "An Experimental Investigation of the Characteristics of Some Plane and Cambered 65º Delta Wings at Mach Numbers from 0.7 to 2.0," ARC RM 3305, 1963, Aeronautical Research Council.